A Method of Estimating Electric Fields above Electrified Clouds from Passive Microwave Observations

MICHAEL PETERSON

Department of Atmospheric Sciences, University of Utah, Salt Lake City, Utah

CHUNTAO LIU

Department of Physical and Environmental Sciences, Texas A&M University–Corpus Christi, Corpus Christi, Texas

DOUGLAS MACH

Science and Technology Institute, Universities Space Research Association, Huntsville, Alabama

WIEBKE DEIERLING AND CHRISTINA KALB

National Center for Atmospheric Research, Boulder, Colorado*

(Manuscript received 16 June 2014, in final form 25 March 2015)

ABSTRACT

A unique dataset of coincident high-altitude passive microwave and electric field observations taken by the NASA ER-2 aircraft is used to assess the feasibility of estimating electric fields above electrified clouds using ubiquitous global and multidecadal satellite products. Once applied to a global dataset, such a product would provide a unique approach for diagnosing and monitoring the current sources of the global electric circuit (GEC).

In this study an algorithm has been developed that employs ice scattering signals from 37- and 85-GHz passive microwave observations to characterize the electric fields above clouds overflown by the ER-2 aircraft at nearly 20-km altitude. Electric field estimates produced by this passive microwave algorithm are then compared to electric field observations also taken by the aircraft to assess its potential future utility with satellite datasets. The algorithm is shown to estimate observed electric field strengths over intense convective clouds at least 71% (58%) of the time over land and 43% (40%) of the time over the ocean to within a factor of 2 from 85-GHz (37 GHz) passive microwave observations. Electric fields over weaker clouds can be estimated 58% (41%) of the time over land and 22% (8%) of the time over the ocean from 85-GHz (37 GHz) passive microwave observations. The accuracy of these estimates is limited by systematic errors in the observations along with other factors. Despite these sources of error, the algorithm can produce reasonable estimates of electric fields over carefully selected individual electrified clouds that differ from observations by less than 20 V m^{-1} for clouds that produce 200–400 V m^{-1} electric fields at 20 km.

1. Introduction

Thunderstorm electrification is an essential component of the global electric circuit (GEC; Williams 2009). Convective clouds generate substantial quantities of charge through collisions between small ice particles and larger graupel pellets in the presence of supercooled liquid water droplets. This process is known as the noninductive charging (NIC) mechanism and has been studied extensively (Reynolds et al. 1957; Takahashi 1978; Jayaratne et al. 1983; Saunders et al. 1991; Saunders and Peck 1998; Takahashi and Miyawaki 2002; Mansell et al. 2005). Vigorous updrafts in convective storms carry smaller ice particles toward the top of the cloud, while larger graupel pellets tend to either remain suspended in the midlevels of the storm or fall toward

* The National Center for Atmospheric Research is sponsored by the National Science Foundation.

Corresponding author address: Michael Peterson, Department of Atmospheric Sciences, University of Utah, 135 S. 1460 E., Rm. 819, Salt Lake City, UT 84112-0102.
E-mail: michael.j.peterson@utah.edu

DOI: 10.1175/JTECH-D-14-00119.1

the surface. This leads to collisions between ice particles of different masses, wherein electrons are typically transferred from the smaller ice particles to the larger graupel pellets, causing them to become oppositely charged.

Over time, as these electrified ice particles gather in different parts of the storm, a distinct charge distribution takes shape. The charge structure of a typical thunderstorm is often described using a tripole model consisting of a strong negative charge region in the midlevels, a strong positive charge region near the cloud top, and a smaller positive charge region near the base of the cloud (Williams 1989), though observations show that there can be significant deviations from this simple model (e.g., Stolzenburg et al. 1998a, Stolzenburg et al. 1998b). Charge that is generated by storm clouds in the troposphere then acts upon the entire atmospheric electrical circuit by interacting with the highly conductive ionosphere (Wilson 1924), as a battery would drive current in a simple resistor–capacitor (RC) circuit. On a global scale, upward currents produced in stormy regions (Wilson currents; Wilson 1921) are counterbalanced by fair-weather return currents elsewhere, maintaining a quasi-static potential difference between the surface and the ionosphere of around 240 kV (Adlerman and Williams 1996; Markson 2007).

Early support for this view of the GEC came from electric field observations taken aboard the research ships *Carnegie* and *Maud*, which recorded the diurnal fair-weather electric field (the Carnegie curve) throughout their voyages across the globe in the early twentieth century. These electric field measurements were found to exhibit similar diurnal variations in universal time to the recorded number of thunder days (Whipple and Scrase 1936), suggesting that thunderstorms could be the drivers of electric current in the atmosphere. More recently, a number of studies have taken advantage of global lightning observations to verify the similarity between diurnal variations in the Carnegie curve and the diurnal cycle of thunderstorm activity (Blakeslee et al. 1999; Bailey and Blakeslee 2006; Williams 2009; Liu et al. 2010; Mach et al. 2011). The primary issue with using only lightning observations to characterize global current contributions from electrified clouds is that it only takes into account contributions from thunderstorms. However, electrified shower clouds (ESCs) without lightning (Wilson 1921) are also an important current source for the GEC (Mach et al. 2009, 2010; Liu et al. 2010). Additionally, recent studies (Mach et al. 2009, 2010, 2011; Blakeslee et al. 2014) suggest that there is a difference in Wilson current strength between oceanic storms and storms over land on a per flash and mean current basis. To improve the agreement between the diurnal lightning activity and the Carnegie curve, recent studies have used high-altitude aircraft retrievals of above-cloud Wilson currents to correct the lightning-based analogs of global electricity (Mach et al. 2011).

Another limitation of these global lightning-based approaches is that they provide only an ensemble view of Wilson currents and the GEC. Like the original curve derived from Carnegie observations, these modern variants are only applicable on annual and seasonal time scales (Mach et al. 2011; Blakeslee et al. 2014). As such, they are not an appropriate tool for examining the finer details of global electricity, such as how different storm types (e.g., isolated convection, MCS's, hurricanes, winter storms), storm regions (e.g., stratiform clouds, charged anvils), and ESCs individually contribute to the GEC. Nor can they describe the GEC on subseasonal time scales. The goal of this study is to develop a method for directly estimating electric fields above individual electrified clouds from common 37- and 85-GHz passive microwave observations. By coalescing the long record of satellite passive microwave observations at or near these frequencies taken by the Special Sensor Microwave Imager (SSM/I; Hollinger et al. 1990), Tropical Rainfall Measuring Mission (TRMM) Microwave Imager (TMI; Kummerow et al. 1998), and Global Precipitation Measurement (GPM) Microwave Imager (GMI; Smith et al. 2007), such an algorithm will make it possible to examine the distribution of global current sources to the GEC on a variety of time scales spanning a time period of more than 27 years as well as study electricity from features ranging from individual clouds to El Niño–Southern Oscillation (ENSO) events.

The basic assumption of the algorithm developed in this study is that cloud ice processes are the primary source of cloud charge. The amount of charge generated should be a function of the frequency of collisions between ice particles, which depends in part on the amount of ice in the cloud. These assumptions are supported by good relationships between lightning flash rate and ice water mass estimated from ground-based and spaceborne radar observations (Deierling and Peterson 2008; Liu et al. 2012). Evidence from aircraft electric field measurements in and around charged anvils also indicates that electric field strength is related to the radar reflectivity structure of electrified cloud regions (Dye and Willett 2007; Dye et al. 2007). Satellite passive microwave brightness temperatures at 37 and 85 GHz have been shown to be directly related to the column-integrated ice water path (Vivekanandan et al. 1991), and passive microwave observations at these frequencies also correlate well with lightning activity (Toracinta et al. 2002; Liu et al. 2011; Prigent et al. 2005; Blyth et al.

2001; Cecil et al. 2005). Therefore, passive microwave observations at these frequencies may be good predictors for cloud electricity. Strong passive microwave ice scattering signals imply an abundance of ice, more frequent collisions, and a greater potential for charge generation, resulting in stronger electric fields above the cloud and greater current contributions to the GEC.

Following this idea, the algorithm uses 37- and 85-GHz passive microwave observations to attempt to infer reasonable estimates of coincident electric field observations. The procedure for estimating electric fields above electrified clouds from passive microwave data and validating the resulting estimates can be broken down into three parts: quality control of the observations and development and application of the electric field estimation algorithm using the quality-controlled data, which will be discussed in section 2, and assessment of algorithm performance in both a statistical context and for individual cases, which will be discussed in section 3.

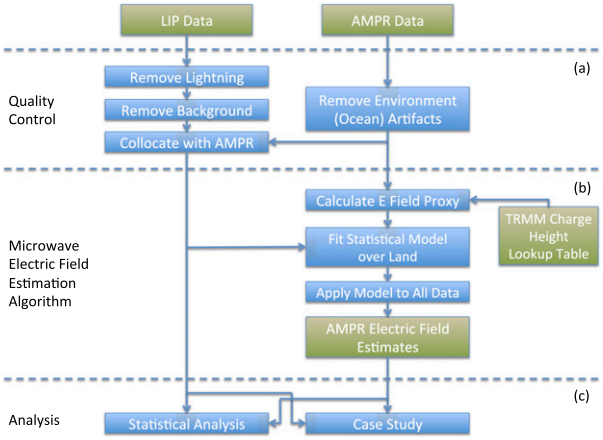

FIG. 1. Schematic diagram of the procedure followed in this study, including (a) data management and quality control steps, (b) algorithm processing steps, and (c) analysis and algorithm assessment steps.

2. Data and methodology

High-altitude aircraft observations taken by the NASA ER-2 aircraft during four different field campaigns are employed in this study. These field campaigns include the third and the fourth Convection and Moisture Experiments (CAMEX-3 and CAMEX-4, respectively; Kakar et al. 2006), the Tropical Cloud Systems and Processes (TCSP) mission (Halverson et al. 2007), and the Tropical Rainfall Measuring Mission Large-Scale Biosphere–Atmosphere Experiment (TRMM-LBA; Halverson and Rickenbach 2002). The benefit of using multiple field campaigns is that each campaign has a different focus and region of interest. Therefore, a wide variety of storms can be examined between these field campaigns. CAMEX-3 took place from July through September of 1998 over the western portion of the Atlantic hurricane domain and includes overflights of Hurricanes Bonnie, Danielle, Earl, and George at different stages of development. The next experiment in the CAMEX series, CAMEX-4, took place over the same region in 2001 and sampled Hurricanes Erin, Gabrielle, and Humberto. TCSP took place around Costa Rica in 2005 and includes overflights of Hurricanes and Tropical Storms Dennis, Emily, and Gert. Each of these three field campaigns includes overflights of numerous oceanic convective and stratiform clouds, as well as some observations over land. Finally, TRMM-LBA was a ground validation mission for the TRMM program conducted in the Brazilian Amazon from the November of 1998 through the February of 1999, which focused on characterizing the dynamical, microphysical, electrical, and diabatic heating characteristics of Amazonian tropical convection.

Observations from two different sensor packages aboard the NASA ER-2 aircraft during these field campaigns are used: electric fields from the Lightning Instrument Package (LIP; Bateman et al. 2007) and passive microwave observations at 37 and 85 GHz from the Advanced Microwave Precipitation Radiometer (AMPR; Spencer et al. 1994). The complete methodology employed in this study is shown in Fig. 1. The first step (Fig. 1a) is to create a collocated dataset of quality-controlled LIP and AMPR observations. A number of quality control measures are applied to both LIP electric fields and AMPR microwave brightness temperatures. These quality control measures are described in section 2a. The second step (Fig. 1b) is the development and application of the electric estimation algorithm. The algorithm consists of three processing steps and requires a lookup table derived from TRMM satellite data. The development and application of the algorithm to quality-controlled LIP and AMPR observations is described in section 2b. Finally, the third step (Fig. 1c) of assessing the performance of the algorithm is described in section 3.

a. The ER-2 high-altitude aircraft combined dataset

The first instrument used in this study, LIP, consists of six or more high-precision electric field mills and an air conductivity probe, which allow the three-dimensional electric field vectors and, with some simple symmetry assumptions, the strengths of Wilson currents to be computed. The field mills have a broad dynamic range, extending from $1.9\,\mathrm{V\,m^{-1}}$ to $1.1\,\mathrm{MV\,m^{-1}}$ (Bateman

et al. 2007; Mach and Koshak 2007), making it possible to observe electric fields as low as the background fair-weather fields up to those generated by nearby electrified clouds and nearby lightning. LIP observations at a sampling rate of $1\,s^{-1}$ are used in this study, which leads to a spatial resolution of 210 m between samples at the nominal cruising speed of the ER-2 (Mach et al. 2009).

To examine electric fields induced by electrified clouds, it is first necessary to filter out electric field responses to other sources, including instrument offsets, and charge on the aircraft. Since LIP only detects the presence of nearby lightning and not which cloud is producing lightning, lightning signals are also removed. This is done in two steps: first, lightning flash signals are removed by eliminating data points between sudden electric field changes of greater than $50\,V\,m^{-1}\,s^{-1}$; then, the long-term average electric field—computed only while the aircraft is flying over clear-air regions between electrified clouds—is subtracted from the remainder of the record. These steps make it possible to compare electric fields generated by different electrified clouds on different flights, days, years, and regions of the world on an equal footing. This method does not remove all sources of error and artifacts from distant and long-lasting lightning events (a single long-lived flash or a high-flash-rate storm) can occasionally still be observed. The overall effect of this filter is to remove virtually all flashes that produce strong electric fields compared to the electrified cloud and most moderate and weak flashes. The flashes that are not properly removed by the filter tend to produce electric fields on the same order of magnitude as the relatively steady electric fields from overflown clouds and manifest themselves as narrow peaks embedded within a broader electric field feature. Because of their modest amplitudes and relative rarity in the filtered sample, lightning artifacts do not significantly affect the quality-controlled LIP statistics, but they may be observable in individual cases.

In addition to lightning concerns, sometimes the background electric fields can be quite strong or instrument offsets can be quite high. In such cases the overall electric field values can be reduced by $60\,V\,m^{-1}$ compared to the raw LIP observations. Determining signals from electrified clouds can be considerably difficult in situations where changes in electric field strength around electrified clouds are on the same order of magnitude as the background value, resulting in a significant amount of uncertainty in weaker electric field observations. For this reason, only electric fields stronger than $10\,V\,m^{-1}$ after employing a background correction are considered in this study.

The second instrument used in this study, AMPR, is a total-power passive microwave radiometer that operates at 10, 19, 37, and 85 GHz. It scans through a 90° scan angle with 50 bins per scan centered at aircraft nadir. While the ER-2 flies at its nominal cruising altitude of 20 km, pixel footprint sizes at ground level range from 640 m for 85 GHz to 2.8 km for 10 GHz. Since scans occur every 3 s, the distance between scans is typically around 630 m while the aircraft is flying at its nominal cruising speed. The overall width of the AMPR swath generally ranges from 30 to 40 km at ground level, depending on the aircraft's attitude and altitude. Observations are continuous for 85 GHz and oversampled for lower frequencies. AMPR is a total-power radiometer that does not report horizontally and vertically polarized brightness temperatures separately. Rather, the polarization of the sensor is a function of scan angle, ranging from completely vertical to completely horizontal at either end of the swath, and an equal measure of each polarization at nadir. Therefore, polarization-corrected temperatures (PCTs; Spencer et al. 1989) cannot be used to correct for observational differences between land and ocean surface backgrounds.

To examine electric field observations in the context of storm structure indicated by coincident microwave observations, LIP electric fields are resampled to match the AMPR record. Collocating LIP observations to the AMPR dataset not only makes it possible to directly compare observations between the two instruments but also provides an opportunity to do further quality control of LIP observations and remove lightning artifacts and missing data. Since LIP has 3 times the temporal resolution of AMPR, a single AMPR observation corresponds to roughly three LIP data points, providing up to three chances to produce a valid collocation. If all LIP observations for a given AMPR data point are valid, then the average is calculated and recorded. However, if any of these LIP data points contain an error code or are marked as an artifact, then they are omitted and the remaining data are considered.

Figure 2 shows an example overflight of an Amazonian thunderstorm observed during TRMM-LBA. AMPR passive microwave observations taken over the storm are shown in Figs. 2a and 2b along with the aircraft flight track. Comparisons between LIP-observed electric fields and near-aircraft-nadir (within 10 AMPR pixels or roughly 6–12 km) minimum AMPR brightness temperatures are shown in Figs. 2c and 2d. The ER-2 flies over two convective features: first, a weaker western feature, and then a stronger eastern feature that forms part of a larger multicell storm. Electric field strengths approach $240\,V\,m^{-1}$ over the first feature, dip to $210\,V\,m^{-1}$ between cells, and then increase to $320\,V\,m^{-1}$ over the second feature. Each of these electric field peaks roughly corresponds to a minimum in near-nadir

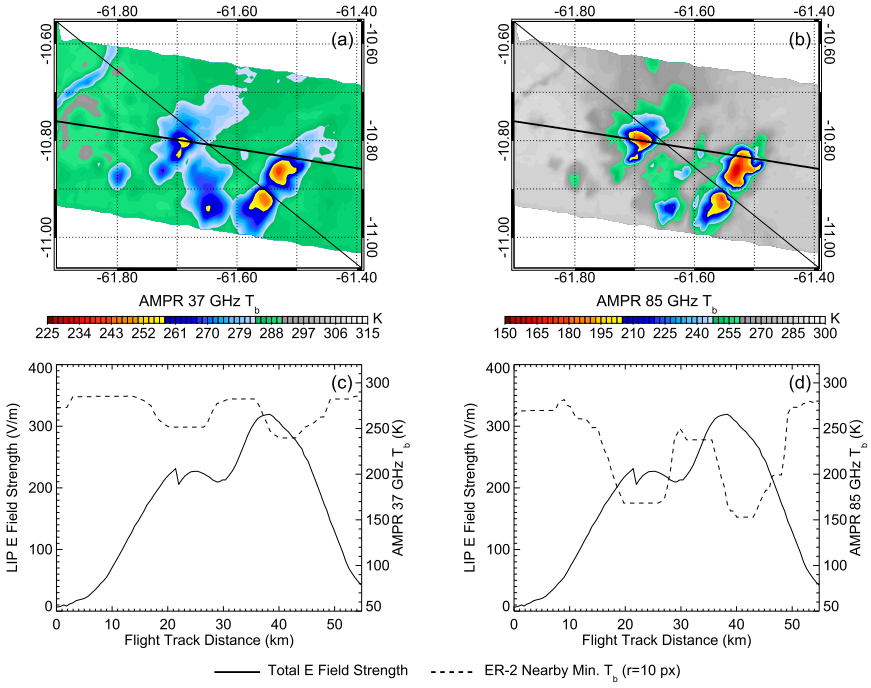

FIG. 2. AMPR (a) 37- and (b) 85-GHz brightness temperatures (contour) observed as the ER-2 flew eastward over a storm in the Amazon. Nearby minimum (c) 37- and (d) 85-GHz brightness temperatures relative to the ER-2 and LIP electric field strengths along the flight track [solid line in (a) and (b)] are shown.

AMPR brightness temperature. Moreover, brightness temperature depressions are greater for the stronger feature with higher electric fields overhead than for the weaker feature, strengthening the case that ice scattering signals may, indeed, be correlated to above-cloud electric field strength.

Table 1 shows the distribution of collocated AMPR scans/LIP observations by field campaign. The largest contributor of raw data to this study is CAMEX-3, which accounts for 40% of all observations. The remaining field campaigns each contribute roughly 20% to the total record. However, a large fraction of these CAMEX-3 data points is erroneous, either consisting of AMPR error codes or LIP lightning artifacts. Once these are removed, the amount of usable CAMEX-3 data is more in line with the other field campaigns. CAMEX-3, CAMEX 4, and TCSP observations occur primarily offshore, while TRMM-LBA observations occur primarily over land. The offshore field campaigns, however, do contribute significantly to the land-based total with more than 15 000 data points between them. Overall, there are 208 550 valid AMPR-/LIP-collocated observations in the sample: 136 800 data points over the ocean and 64 991 over land, corresponding to an aggregate total of approximately 173 h of flight time or 13 000 km traversed by the ER-2 aircraft. These numbers include both overflights of thunderstorms and clear-air regions while the aircraft was in transit to a particular storm of interest with the instruments turned on.

b. *Microwave estimates of above-cloud electric fields*

A simple model is constructed to estimate aircraft-altitude electric fields from 37- and 85-GHz passive microwave brightness temperatures based on coincident ER-2 LIP and AMPR measurements. Calculations are conducted separately for each frequency, resulting in two independent electric field estimates that share the same theoretical foundation and are subject to the same simplifying assumptions and approximations. Consider an example overflight of an idealized thunderstorm with a typical tripole charge structure as shown in Fig. 3a. The polarities of the charged ice particles within the storm and

TABLE 1. Distribution of collocated AMPR and LIP observations by field campaign and by land and ocean.

		With valid AMPR and LIP observations				
Field campaign	Total	Total	Land	(%)	Ocean	(%)
CAMEX 3	101 684	64 152	6972	10.8	57 180	89.2
CAMEX 4	47 396	45 699	1122	2.4	44 577	97.6
TCSP	50 914	48 850	7057	14.4	41 777	85.6
TRMM-LBA	55 826	49 849	49 840	100	9	0
Total	255 820	208 550	64 991	31.1	143 543	68.8

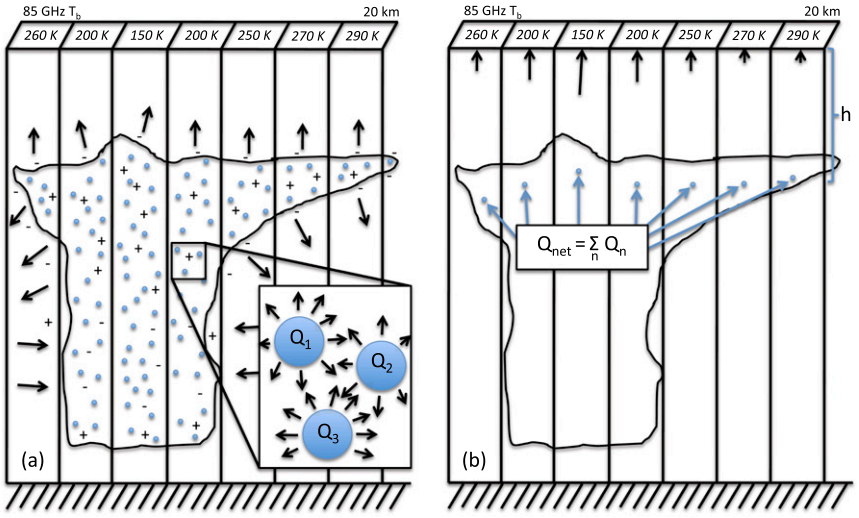

FIG. 3. Conceptual diagram of (a) the electrical structure and 85-GHz brightness temperatures of a thunderstorm and (b) how it is simplified in the algorithm.

the orientations of electric field vectors at various locations are shown as well as 85-GHz passive microwave brightness temperatures taken along a trajectory over the storm. Charge generation mechanisms in this conceptual storm have led to a buildup of positively and negatively charged particles in different parts of the storm, creating regions of net positive and net negative charge. To complicate the picture further, in this example the buildup of strong charge regions has also led to the creation of oppositely charged screening layers along the storm's boundaries.

Determining the net electric field at an arbitrary point within the storm analytically would be difficult and would require information about the strengths and locations of individual charge sources throughout the storm. Even along the storm's boundaries, the net electric field vectors (arrows in the figure) change direction frequently. Fortunately, the GEC is only dependent on the net effect of these charges and the resulting currents they produce out the tops of electrified clouds. In this context, the problem can be simplified (Fig. 3b) and approximated as a layer of net charges (Q_i) (e.g., Driscoll et al. 1992, 1994) that summarizes the overall effect each of the charge regions within their respective sample volumes has on the Wilson currents out the top of the cloud. In this scenario, the electric fields at an altitude far above the cloud (arrows) can be calculated by integrating Coulomb's law [(Eq. (1)] across the layer of net charges,

$$|E_i(r_i)| = k_e \frac{|Q_i|}{r_i^2}, \tag{1}$$

where E_i is the electric field resulting from net charge Q_i, r_i is the distance between the net charge source and the observer, and k_e is Coulomb's constant. Following this conceptual model, if the relative strengths and altitudes of net charges for a given storm can be approximated using passive microwave observations, then electric fields at an arbitrary distant altitude above an electrified cloud can be computed using a Coulomb integration of microwave data and a scaling function to fit the results to observations.

Both of these unknown parameters may be different for convective and different types of nonconvective clouds (e.g., anvils, mature stratiform clouds), which not only have very different physical structures but also electrical characteristics. These differences must be taken into account in order to properly characterize electricity from storm regions outside of the convective core. Nadir-pointing radar observations also taken aboard the ER-2 aircraft are also available and would be able to provide some information about the vertical structure of the storm regions directly below the aircraft, but since the algorithm integrates over the entire AMPR domain such observations would not be of much benefit. For the purposes of this study to show if it is possible to formulate any relationship between passive microwave and electric field observations, all clouds will instead be treated as convective while recognizing that estimated electric fields over clouds that may not be convective could be subject to significant errors. Future work will then use ground-based radars, where available, to tune the algorithm to handle different types of clouds and storm regions.

The first task in creating the algorithm is to characterize the height of the layer of net charges relative to the aircraft. Since Coulomb's law varies by distance

squared, large errors in this charge layer height can have a significant impact on the resulting electric field estimates. The aircraft altitude can be read off the altimeter, but the altitude of the net charge layer remains an unknown. Previous studies assign constant values for the height of the upper positive charge layer responsible for Wilson current generation (Driscoll et al. 1992). Prescribing a single value for the net charge layer height, however, does not take into account variations in storm height for storms of differing convective intensity. For instance, a 10-km charge layer height may be appropriate for an intense thunderstorm over land with strong radar echoes up to 14 km, but it would not properly describe a weaker storm whose strongest echoes only exceed the freezing level by a few kilometers.

A more realistic approach would be to allow the net charge layer height to vary with the strength of the passive microwave signal at each point. Weak convection and stratiform regions with only modest microwave brightness temperatures would then have lower net charge layer heights than strong convection with strong passive microwave signals and strong updrafts capable of lofting charged ice particles to higher altitudes. The challenge then becomes to determine what would be an appropriate altitude for the height of the net charge layer that characterizes this variance in convective intensity.

For a conceptual storm with a negative charge layer at 5 km and an equally strong positive charge layer at 10 km, the upper charge layer is the most relevant charge layer for above-cloud electric fields due to its proximity to the cloud top. In this scenario, Coulomb's law indicates that the contributions of the upper positive layer to the 20-km electric fields are 2.25 times greater compared to the lower negative layer. However, both charge layers influence the resulting electric fields. For this reason, it would seem reasonable to assign the height of the net charge layer somewhere in between the two layers but perhaps weighted to be closer to the upper positive layer of charge.

One possible measure of net charge layer height then is the highest altitude with a radar graupel signature. Graupel is typically a carrier of negative charge, so the highest altitude where graupel is detected roughly corresponds to the very top of the negative charge layer just below the positive charge layer. As 30-dBZ radar echoes are often used as an indicator of the likely presence of graupel and 30-dBZ echoes have been shown to relate well with lightning activity (Marshall and Radhakant 1978; Peterson 2011; Liu et al. 2012), 30-dBZ echo-top heights seem to be a satisfactory net charge layer height approximation that would vary with storm intensity.

However, radar observations are not always available, so a lookup table relating 30-dBZ echo-top heights to passive microwave observations must be constructed. Figure 4 shows two-dimensional histograms of coincident 30-dBZ echo-top height and passive microwave polarization-corrected brightness temperature observations from the TRMM satellite over land and ocean regions. A crude lookup table is created by recording the mean echo-top height for various microwave signal strengths (solid lines). The histograms show a considerable spread due to beamfilling issues (Nesbitt et al. 2000) and the fact that TRMM observations represent the properties of a wide variety of storms. However, this method does produce a reasonable observations-based variance in the net charge layer height for land and ocean storms of differing convective intensity. Charge layer heights in this lookup table vary from 7 km for the weakest passive microwave signals to nearing 15 km for the absolute strongest. Variations between these two extremes are roughly described as a linear relationship for 85 GHz and a logarithmic relationship for 37 GHz.

Using this approach, the Amazonian storm shown in Fig. 2 can be represented as a series of net charges as in Fig. 5. In this figure, each AMPR pixel corresponds to a single net charge (dot) in the figure. Environmental pixels surrounding the primary storm regions have been filtered out, leaving net charge features that vary in height between 8- and 11-km altitude. The extent and distribution of net charges within each feature varies between each frequency depending on the strength of the corresponding microwave signals. The stronger convective feature to the east has similar charge heights at 37 and 85 GHz in the main convective region, but charge heights in the smaller feature to the west are more than 1 km lower at 37 compared to 85 GHz. This is possibly due to a smoothing effect stemming from the larger 37-GHz pixel size.

The second task is to relate passive microwave observations to bulk charge accumulation. This is not straightforward, however. Without coincident observations for side-by-side comparison, the most attractive method of creating such a relationship becomes a guess-and-check approach, where arbitrary transfer functions are constructed and compared to LIP electric field observations to see how well they fit the data. Fortunately, it is possible to infer some details on the nature of this relationship from theory and use this information as guidance. Passive microwave

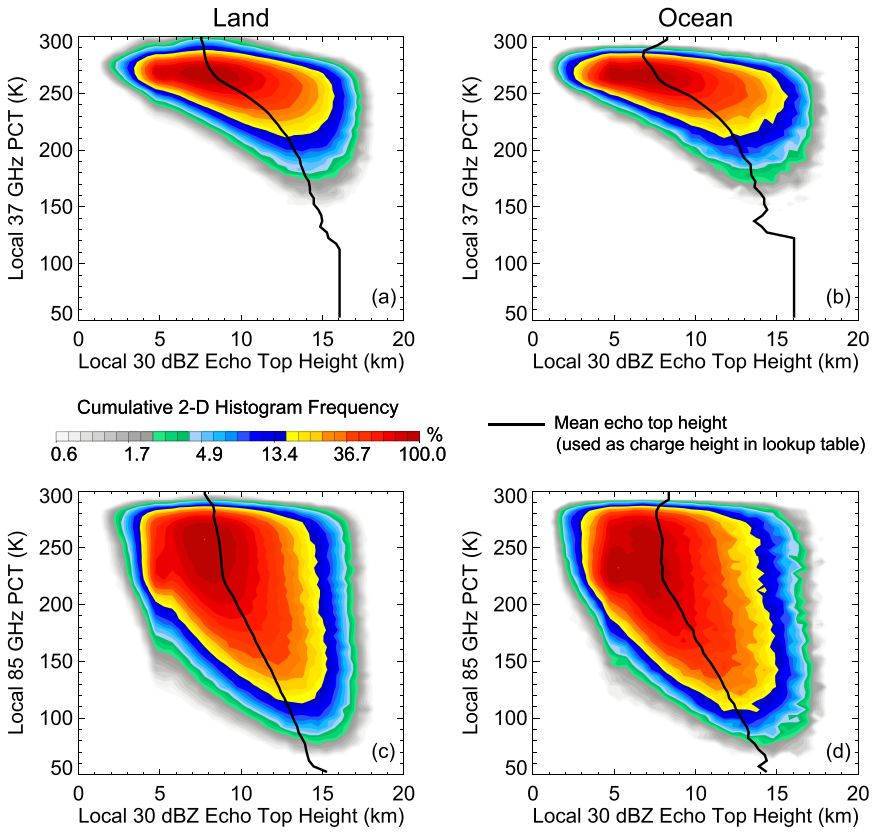

FIG. 4. Two-dimensional histograms of TRMM PR 30-dBZ echo-top height and coincident (a),(b) 37-GHz PCT and (c),(d) 85-GHz PCT for land and ocean regions around the globe. The net charge layer height lookup tables for each region and frequency are shown as solid lines.

observations at 37 and 85 GHz are sensitive to the amount of ice in the column below. Since noninductive charge generation involves collisions between ice particles, it should follow that more ice leads to more frequent collisions and more charge generated. Therefore, the relative strength of each net charge should be a direct function of the strength of the corresponding microwave signal. Functions chosen for examination are of the form

$$f = (T_{b\mathrm{env}} - T_b)^n, \tag{2}$$

where $T_b - T_{b\mathrm{env}}$ is the microwave brightness temperature depression from an environmental value and

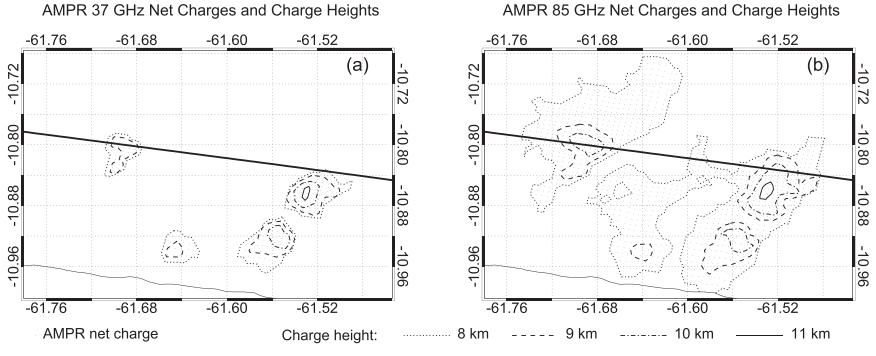

FIG. 5. Distribution of (a) 37- and (b) 85-GHz net charges and charge layer heights in the example case shown in Fig. 1.

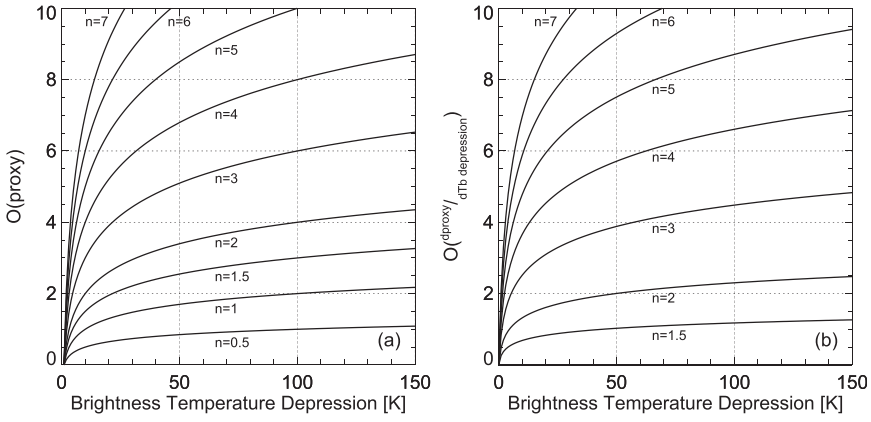

FIG. 6. Orders of magnitude of (a) proxy values and (b) derivatives of candidate functions considered in this study with exponents (p values) ranging from 0.5 to 7.

values of n range from 0.5 to 7. Figure 6 shows the orders of magnitude of proxy function output for each value of n (Fig. 6a) and their derivatives (Fig. 6b) across a typical range of microwave brightness temperature depressions. Two additional criteria are introduced to assess the feasibility of each candidate function:

1) The desired function should emphasize the difference between weak convection or stratiform clouds and strong convection.
2) The desired function should produce similar values across small variations in brightness temperature depression (and by extension, column ice content) in order to reduce the amount of uncertainty in the results.

In other words, the difference in proxy output between large and small brightness temperatures in Fig. 6a should be maximized while keeping the derivatives in Fig. 6b reasonably low. Plotting each candidate proxy function against LIP electric field observations (not shown for all values of n) reveals that functions between $n = 2$ and $n = 4$ produced histograms with the lowest variance such as those shown in Fig. 7 for $n = 2$ over land. For values of n within this range, the higher-power functions produced estimates that handled weak electric fields in stratiform regions better, but at the expense of having a higher variability in estimated electric field strength between storms with similar microwave brightness temperatures. A greater consistency between similar estimates was deemed to be the more desirable result, so the $n = 2$ function was chosen for analysis. Statistical models were then constructed to scale proxy values at each frequency over land to observations (dotted lines in Fig. 7). This model is a simple fit to the median line for each distribution to ensure that each passive microwave prediction would be centered within the distribution of observations associated with that value.

Attempts to apply the same methodology to AMPR observations over the ocean are limited by the fact that microwave emissivity differs greatly between land and ocean. Emissivity over the ocean is also affected by highly variable factors, such as sea-foam and sea surface roughness (Hwang 2012), resulting in not only drastic differences in clear-air microwave brightness

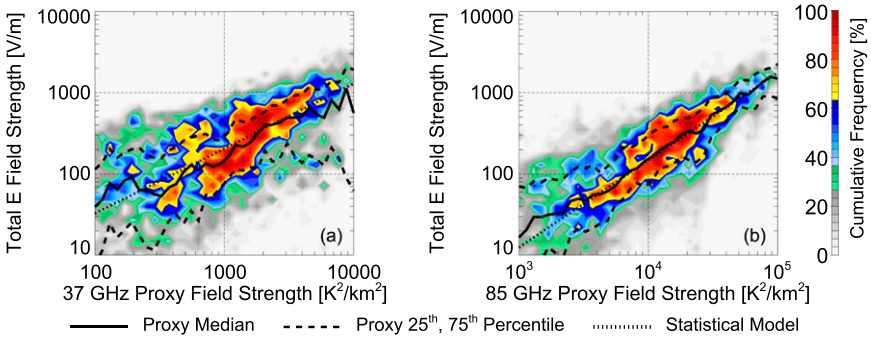

FIG. 7. Normalized two-dimensional histograms of (a) 37- and (b) 85-GHz proxy values and observed electric fields over land. Quartile plots (dotted and dashed lines) and statistical fits (dotted line) are overlaid.

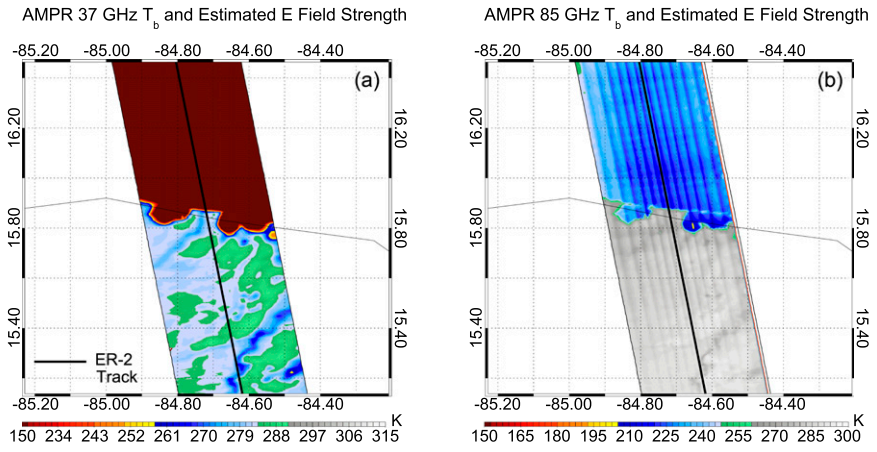

FIG. 8. AMPR (a) 37- and (b) 85-GHz brightness temperatures (contour) observed as the ER-2 flew northward across a coastline. LIP electric field observations and microwave estimates using (c) 37- and (d) 85-GHz AMPR observations without environmental filtering along the flight track [solid line in (a) and (b)] are shown.

temperatures between land and ocean as seen in Figs. 8a and 8b, but also significant regional differences over the ocean and temporal differences for the same ocean region under different conditions.

This variability makes it difficult to separate the background environment from truly cloudy regions over the ocean, which is a necessary step for constructing an ocean-based statistical model to fit proxy values to observed electric fields. In contrast to observations over land, where ice-laden clouds appear as low brightness temperature features against a warm background, clouds over the ocean are observed as warm valleys surrounded by a highly variable and cold brightness temperature background. Ocean surface passive microwave observations can resemble moderate convection at 85 GHz (~220 K) and resemble some of the most intense convective cases observed over land at 37 GHz (~150 K). Because of the vastness of the ocean surface and the coldness of the microwave brightness temperatures observed overhead, if any significant portion of the ocean surface is misidentified as a cloud by the environmental filter, then it would introduce a substantial amount of error in nearby electric field estimates. This issue could be eliminated by calculating polarization-corrected temperatures from independent horizontally and vertically polarized observations, but since AMPR does not provide separate measurements for each polarization, this source of error cannot be effectively filtered for all ocean regions.

To gauge the significance of this problem, distributions of proxy values and LIP observations over the ocean are shown in Fig. 9. These histograms have significantly more spread compared to the land distributions in Fig. 7, particularly on the high end of proxy field values for a given LIP-observed electric field strength. This is especially true for the 37-GHz estimates, which show no correlation at all between the two parameters, since the signal is completely washed out by cold ocean surface errors.

The estimated electric field using the land-based model is overlaid for comparison with Fig. 7. While 37-GHz

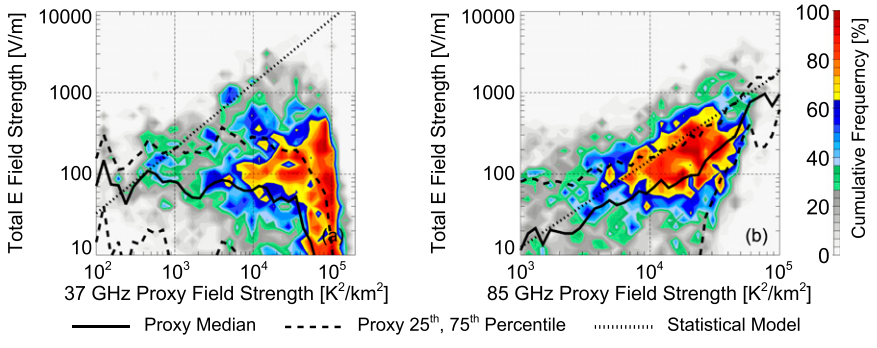

FIG. 9. Normalized two-dimensional histograms of (a) 37- and (b) 85-GHz proxy values and observed electric fields over the ocean. Quartile plots (dotted and dashed lines) and land-based statistical fits (dotted line) are overlaid.

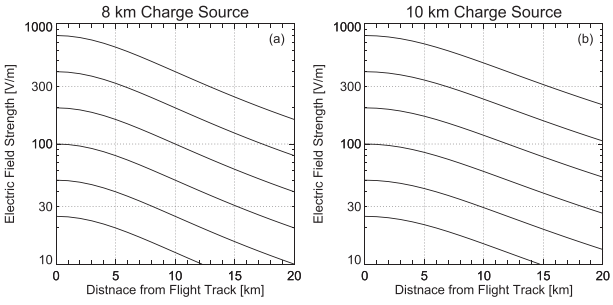

FIG. 10. Electric fields at aircraft position ($x = 0$) and altitude (20 km) as point charges that produce various electric fields at aircraft nadir and (a) 8 km and (b) 10 km altitude are moved away from the aircraft to the edge of the AMPR swath ($x = 20$ km).

estimates are entirely biased by this effect, the land-based model does seem to characterize a significant, though not substantial, number of oceanic data points at 85 GHz. Moreover, since the land-based model parallels the upper boundary of the 85-GHz distribution, where data points are likely not significantly biased by mislabeled open ocean regions, it may be possible that the model would work well with both land and ocean data if this effect could be removed completely. However, given the high level of variability in these estimates, the ability of the land-based model to estimate oceanic electric fields will have to be assessed in individually selected cases with minimal ocean surface bias.

Another potential source of error in the data that should be discussed is the issue of missed events. While AMPR samples the atmosphere directly below the aircraft within a narrow swath, LIP is sensitive to any nearby electrical source. This can lead to higher electric field observations than what may be indicated by AMPR, leading data points to be spread along the left side of the histograms in Figs. 7 and 9. To gauge how much of an impact nearby electrified clouds outside the AMPR field of view can have on LIP observations, charges of varying strengths and altitudes are placed below the aircraft and then moved from aircraft nadir to the edge of the AMPR swath. Resulting electric fields as a function of the horizontal distance between the charges and ER-2 nadir are shown in Fig. 10. Charges that produce electric fields exceeding 50 V m^{-1} directly overhead assuming an 8-km charge height or 40 V m^{-1} assuming a 10-km charge height would produce electric fields exceeding 10 V m^{-1} at the edge of the AMPR swath, the minimum LIP observational threshold that is assumed valid in this study. A storm with moderate electric fields just over 300 V m^{-1} like the one in Fig. 2 could still produce significant electric fields of nearly 100 V m^{-1} if it were positioned at the edge of the AMPR swath. This scenario could potentially double the perceived electric field from a typical electrified cloud or indicate significant electrical activity in an apparent clear-air region below the aircraft. Stronger storms could even occur entirely outside of AMPR's field of view and still dominate the LIP signal. Fortunately, the apparent correlations between LIP electric field strengths and proxy values in Fig. 7 (and to a lesser extent in Fig. 9b) imply that the error induced by this effect is limited in most cases, but it undoubtedly contributes to the overall error in the algorithm's estimates.

3. Results

a. *Assessment of passive microwave electric field estimates*

The land-based statistical models are applied to electric field proxy values calculated over both land and ocean, and the resulting microwave electric field estimates are compared to LIP observations in Fig. 11 (land) and Fig. 12 (ocean). The overall distribution of data points is shown as a color contour two-dimensional

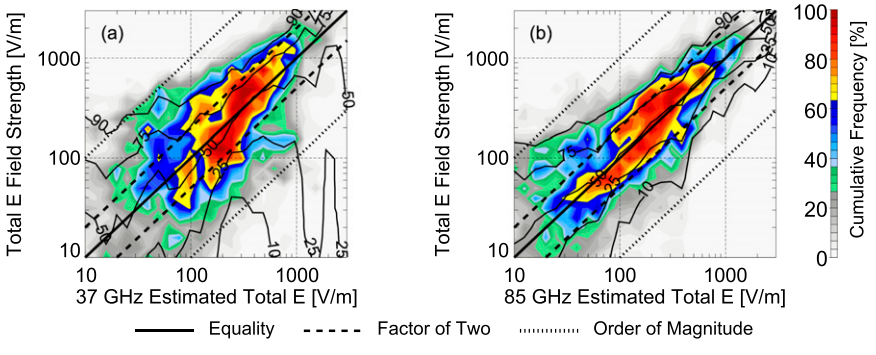

FIG. 11. Normalized two-dimensional histograms of (a) 37- and (b) 85-GHz estimated electric field strength and observed electric field strength over land (color contours). CFDs of LIP electric field strengths are produced for each range of algorithm estimate, and contour plots of various percentiles are overlaid (line contours). Diagonal lines representing various error levels are also shown.

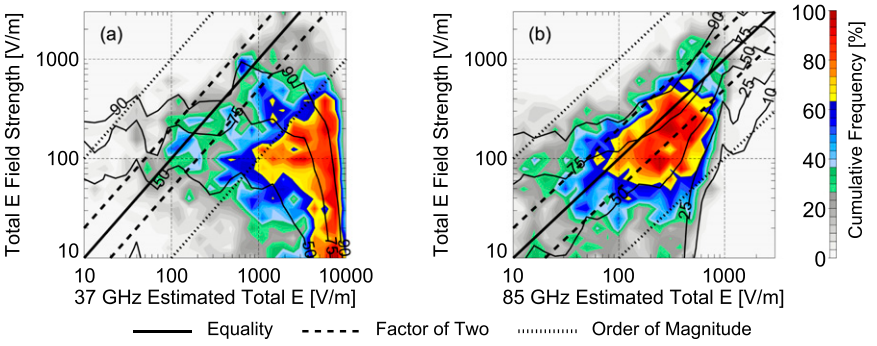

FIG. 12. Normalized two-dimensional histograms of (a) 37- and (b) 85-GHz estimated electric field strength and observed electric field strength over the ocean (color contours). CFDs of LIP electric field strengths are produced for each range of algorithm estimate, and contour plots of various percentiles are overlaid (line contours). Diagonal lines representing various error levels are also shown.

normalized histogram in each figure panel. A line contour plot representing cumulative frequency distributions (CFDs) of LIP observations for a given microwave estimate value is overlaid. Diagonal lines signifying various levels of disagreement between observations and estimates are also shown.

Despite the significant potential for systematic errors in the data due to the factors discussed in the previous section, most of the data points using either the 37- or the 85-GHz estimate over land are located near or along the line of equality. The accuracy of the microwave estimates does show some frequency dependence, however. The 37-GHz histogram shows a larger visual spread, indicated quantitatively by a highly variable interquartile range (IQR) for different values of estimated electric field strength. The IQR is smallest for moderate 37-GHz electric field strength estimates ranging from 200 to 500 $V\,m^{-1}$. In contrast, first and third quartiles of observations associated with 85-GHz estimates follow the factor-of-2 error lines across the majority of the figure domain, indicating that the algorithm performance is not dependent on electric field strength.

This significant difference in algorithm performance between the 37- and 85-GHz estimates could be due to the differing AMPR pixel sizes between frequencies (640 m for 85 GHz compared to 1.5 km for 37 GHz) or due to differences in how sensitive each frequency is to ice particles of different sizes. As large ice particles scatter upwelling microwave radiation, higher frequencies would be more sensitive to smaller ice particles than lower frequencies from a size parameter argument. This is why 37-GHz observations are more suitable for use as a hail proxy than 85-GHz observations; 85-GHz observations are still responsive to hail, but since there is more scattering by smaller particles, such as graupel, at this frequency, there is a greater incidence of strong microwave signals at 85 GHz with no corresponding hail reports (Cecil 2009).

The performance of the land-based algorithm suffers over the ocean (Fig. 12), as discussed in the previous section, with most data points falling in the ''false alarm'' category of electric field estimates that exceed observations. Still, comparing the IQRs between the land and ocean distributions indicates that for most 85-GHz estimates, the same range of errors that bounds 50% of the data points taken over land also accounts for 25%–40% of data points over the ocean. This percentage increases with increasing estimated electric field strength, as ocean surface artifacts cause a greater fractional error for weaker electrified clouds than for strong thunderstorms.

Overall algorithm performance categorized by the passive microwave signal strength and observed electric field strength is shown in Table 2 (37 GHz) and Table 3 (85 GHz). Electrified cloud regions are classified in terms of their 85-GHz brightness temperatures as being relatively weak (>260 K), moderate (220–260 K), or intense (<220 K). Only 85-GHz observations are employed in this classification to remove the ocean surface effect. Clouds are also classified as to whether significant electric fields (>100 $V\,m^{-1}$) are observed. For each category, the passive microwave electric field is grouped by land or ocean and whether it falls within a factor of 2 of observations or if it significantly underestimates or significantly overestimates what LIP reports.

At 37 GHz (Table 2), the algorithm predicts electric fields to within a factor of 2 of observations 18.1% of the time, underestimates observations 12.9% of the time, and overestimates observations 69.0% of the time. The 37-GHz estimates favor overestimation because most of the ER-2 data used in this study are taken over the

TABLE 2. Algorithm performance at 37 GHz in terms of mean error (%). Overflown clouds are classified as weak ($T_{b\ 85\ GHz} > 260$ K), moderate (260 K $> T_{b\ 85\ GHz} > 220$ K), and strong ($T_{b\ 85\ GHz} < 220$ K).

	|Error| < 100%	Error < −100%	Error > 100%
Land and ocean			
All data	18.1	12.9	69.0
>100 V m^{-1}	34.4	24.4	41.2
Moderate	12.4	9.5	78.1
>100 V m^{-1}	27.1	21.5	51.5
Strong	47.8	20.5	31.7
>100 V m^{-1}	50.2	21.9	27.9
Land only			
All data	36.3	28.7	35.0
>100 V m^{-1}	48.9	38.4	12.7
Moderate	41.1	33.7	25.2
>100 V m^{-1}	48.3	40.9	10.8
Strong	57.6	26.1	16.3
>100 V m^{-1}	58.1	26.7	15.2
Ocean only			
All data	9.2	5.2	85.7
>100 V m^{-1}	23.1	13.3	63.7
Moderate	7.7	5.4	86.9
>100 V m^{-1}	19.0	13.7	67.3
Strong	39.7	16.6	43.7
>100 V m^{-1}	42.9	18.2	39.0

TABLE 3. Algorithm performance at 85 GHz in terms of mean error (%). Overflown clouds are classified as weak ($T_{b\ 85\ GHz} > 260$ K), moderate (260 K $> T_{b\ 85\ GHz} > 220$ K), and strong ($T_{b\ 85\ GHz} < 220$ K).

	|Error| < 100%	Error < −100%	Error > 100%
Land and ocean			
All data	30.9	27.8	41.3
>100 V m^{-1}	48.8	38.6	12.5
Moderate	27.3	20.5	52.2
>100 V m^{-1}	53.9	34.5	11.6
Strong	55.1	13.2	31.7
> 100 V m^{-1}	58.9	14.3%	26.8
Land only			
All data	44.9	32.3	22.8
>100 V m^{-1}	55.1	37.7	7.3
Moderate	57.7	18.6	23.7
>100 V m^{-1}	68.4	23.0	8.6
Strong	71.2	10.9	17.9
>100 V m^{-1}	71.6	11.2	17.2
Ocean only			
All data	24.4	23.9	51.7
>100 V m^{-1}	44.9	37.8	17.3
Moderate	22.5	18.9	58.5
>100 V m^{-1}	49.2	37.5	13.3
Strong	42.9	14.5	42.5
>100 V m^{-1}	48.3	16.5	35.3

ocean. Over land, the performance of the algorithm at 37 GHz improves significantly such that 36.3% of the data fall within this margin of error. This fraction increases further when only clouds with observed electric fields exceeding 100 V m^{-1} are considered (48.9% over land) as well as for clouds with moderate 85-GHz signals (41.1% over land, 48.3% over land with electric fields > 100 V m^{-1}) or strong convection (57.6% over land,

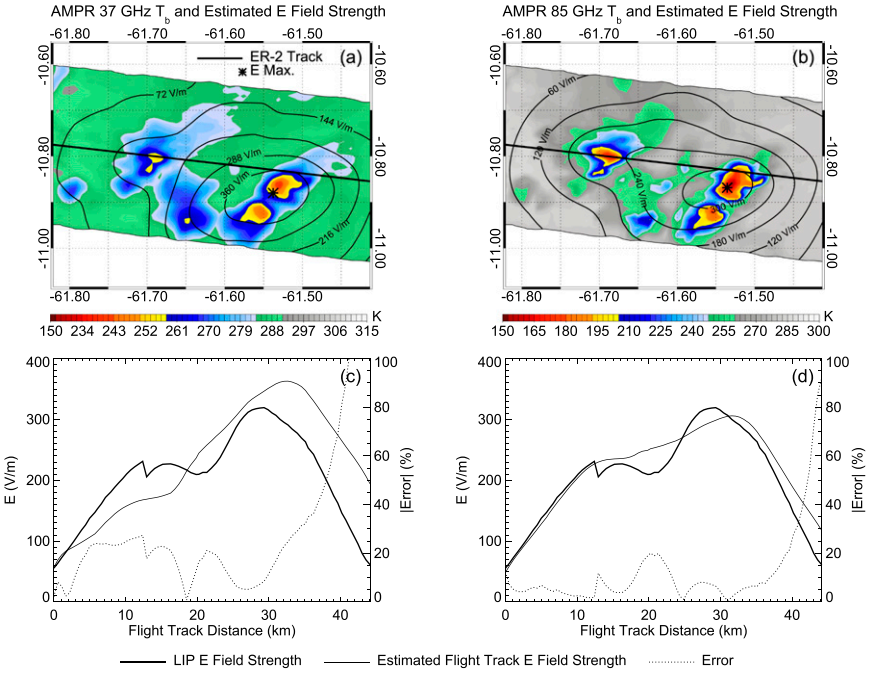

FIG. 13. AMPR (a) 37- and (b) 85-GHz brightness temperatures (contour) observed as the ER-2 flew eastward across the same storm region depicted in Fig. 1. LIP electric field observations and microwave estimates using (c) 37- and (d) 85-GHz AMPR observations along the flight track [solid line in (a) and (b)] are shown.

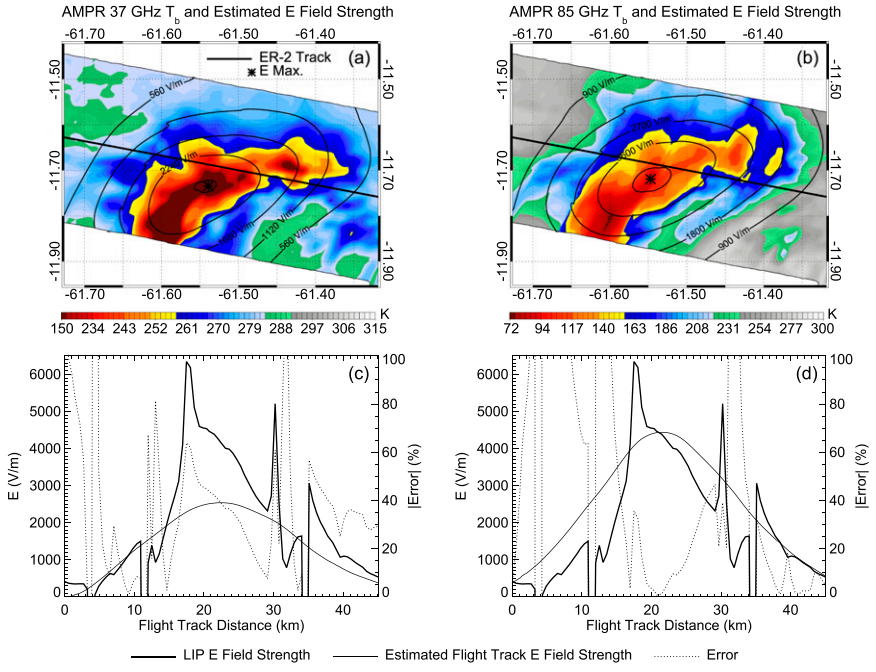

FIG. 14. AMPR (a) 37- and (b) 85-GHz brightness temperatures (contour) observed as the ER-2 flew across an intense Amazonian thunderstorm. LIP electric field observations and microwave estimates using (c) 37- and (b) 85-GHz AMPR observations along the flight track [solid line in (a) and (b)] are shown.

58.1% over land with electric fields $> 100\,\mathrm{V\,m^{-1}}$). The algorithm is more likely to overestimate observations in most categories, except for clouds over land with moderate and strong 85-GHz signals, where it is more likely to underestimate observations.

At 85 GHz (Table 3), the algorithm predicts electric fields to within a factor of 2 of observations 30.9% of the time overall and 48.8% of the time for clouds with observed electric fields exceeding $100\,\mathrm{V\,m^{-1}}$. Each of these fractions increases by 15%–44.9% and 55.1% when only storms over land are taken into account. The algorithm performs the best for clouds over land with moderate 85-GHz signals and strong electric fields or strong convective 85-GHz signals, with or without accompanying strong electric fields. In these cases, the algorithm characterizes as much as 70% of the LIP observations to within a factor of 2. Overall, the algorithm overestimates LIP observations over the ocean and underestimates observations over land and clouds with strong electric fields over either land or ocean.

b. *Case studies*

To put these statistical measures of algorithm performance into perspective considering the assumptions and sources of error that are present, it is necessary to examine how the algorithm handles individual cases. The benefit of a case study analysis is twofold: first, AMPR and LIP observations can be vetted for signs of systematic error, such as unseen nearby convection, that are obvious to the human eye but difficult to diagnose using an automated approach; and second, algorithm performance may be assessed for specific types of storms and storm regions.

Four cases have been selected for discussion that highlight the strengths and weaknesses of the algorithm's estimates: two over land and two over the ocean. The first case is shown in Fig. 13. This case is the same Amazonian storm from Fig. 2, but line contours of estimated electric field strength across the AMPR domain have been added to Figs. 13a and 13b, and flight track electric field estimates have been added to Figs. 13c and 13d for comparison with LIP observations. This case was chosen because all apparent features contributing to the LIP electric field observations were well captured by the AMPR swath. It is also a slightly complex case to examine, as there are multiple features of differing convective intensity that all contribute to the overall electric field.

The contours of estimated electric fields from both frequencies peak over the stronger cell, plateau out to the isolated weaker cell, and then decrease radially outward. Slight differences in the shape of the 37- and 85-GHz contours can be observed in addition to intensity. The electric field peak location, for example, is located between the two cells of the larger eastern

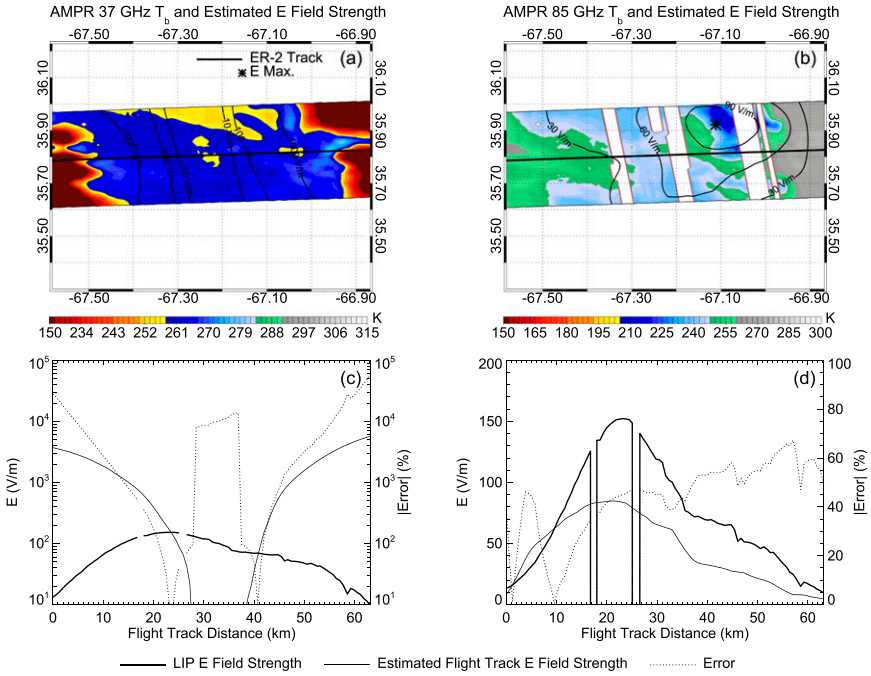

FIG. 15. AMPR (a) 37- and (b) 85-GHz brightness temperatures (contour) observed as the ER-2 flew westward across an oceanic squall line. LIP electric field observations and microwave estimates using (c) 37- and (d) 85-GHz AMPR observations along the flight track [solid line in (a) and (b)] are shown.

feature in the 37-GHz reconstruction, but it is squarely over the stronger northern cell at 85 GHz. Overall, estimates from both frequencies along the ER-2 flight track mirror the shape of the LIP curve reasonably well. However, the 85-GHz estimates appear to be more accurate in this case, reaching peak values that are off by only a few percent. The 37-GHz curve is also apparently more sensitive to the stronger linear feature than the smaller isolated cell. This is because the smaller cell appears to be significantly weaker at 37 GHz compared to the linear feature than at 85 GHz. Despite this, 37-GHz errors remain below 30% throughout the majority of the overflight. Both estimates delay the second observed peak slightly, resulting in higher percent errors near the end of the overflight.

A much stronger TRMM-LBA case is shown in Fig. 14. This Amazonian thunderstorm contains large areas of very strong passive microwave signals and electric fields reaching 4500 V m^{-1} sustained to 6300 V m^{-1} with lightning artifacts that could not be removed by the lightning filter. Given the size and severity of this storm, there is a significant potential for storm regions outside the AMPR swath to influence the LIP observations, but given the strength of the observed electric fields, this effect would only likely contribute a few percent to the total. The 37-GHz electric field estimates in this case are off by 40% of the sustained peak value (outside of the lighting) and 85-GHz estimates are off by less than 10%. Where the 85-GHz algorithm fails to perform in this case is along the flanks, where the observed electric fields drop off faster than the estimates. This could be due to the influence of the large but relatively weak cloud region surrounding the convective core, the presence of strong screening layers, differing charge structures between convective and stratiform precipitation, or some other factor. The algorithm assumes a simple convective charge structure and may therefore fail to characterize electricity above other types of clouds. This will be explored in a future study.

An example oceanic case is shown in Fig. 15. In this case, the ER-2 traversed an eastward-moving storm system over the Atlantic Ocean with a large region of stratiform precipitation during the Convection and Moisture Experiment (CAMEX) 4. Electric fields over this storm reached 150 V m^{-1} over the convective region of the storm to the east and then dropped to around 50 V m^{-1} over stratiform region as the aircraft flew west over the storm. Since this storm occurred over the ocean, 37-GHz estimates are wildly inaccurate. However, 85-GHz estimates mirror the shape of the LIP curve but are 40%–60% lower than observations throughout most of the overflight. Part of the issue is that there are a number of missing AMPR scans, particularly over the convective

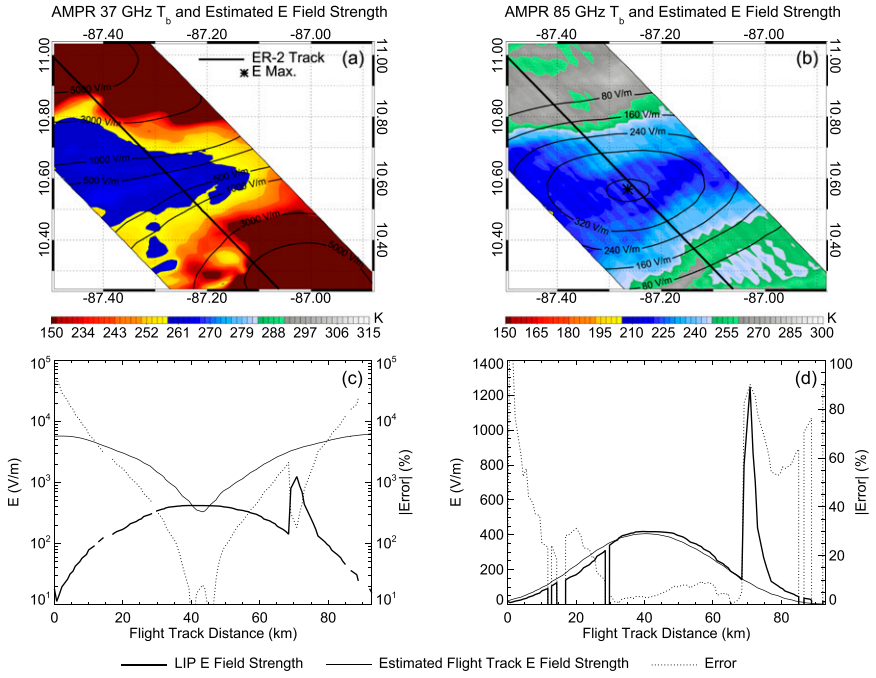

FIG. 16. AMPR (a) 37- and (b) 85-GHz brightness temperatures (contour) observed as the ER-2 flew across a dissipating nocturnal MCS. LIP electric field observations and microwave estimates using (c) 37- and (d) 85-GHz AMPR observations along the flight track [solid line in (a) and (b)] are shown.

part of the storm. If adding this missing information would have the effect of doubling the 85-GHz estimates, then they would resemble observations despite the more stratiform nature of this case. However, even without these scans, errors are still within the factor-of-2 margin of error used previously.

Figure 16 shows an example of a stronger oceanic storm that produced electric fields exceeding 400 V m^{-1} observed during TCSP on 20 July 2005 near the end of the flight, when the ER-2 aircraft was flying over a dissipating yet still electrically active nocturnal MCS with high lightning flash rates. This oceanic storm region is broad yet relatively weak, with 85-GHz brightness temperatures above 200 K filling the entire AMPR swath. Once again, the 37-GHz estimates are biased by the ocean surface, but the 85-GHz estimates agree rather well with observations. The only exceptions are where there are missing data or the lightning artifact. Aside from these instances, the 85-GHz estimate matches the observed amplitude of this oceanic event to within a few volts per meter throughout the overflight, despite the fact that these estimates use the model that was developed over land.

4. Conclusions

A method for estimating above-cloud electric fields using passive microwave observations is presented and its performance is assessed statistically and with individual cases. The eventual goal for this work is to apply such an algorithm to multiple decades of satellite passive microwave observations in order to diagnose the global distribution of charge sources that drive the global electric circuit and to examine input into the GEC on scales ranging from individual electrified clouds to ENSO events.

Even though certain sources of error inherent in the data cannot be eliminated, the algorithm has been shown to produce estimates using 85-GHz (37 GHz) brightness temperatures that fall within a factor of 2 compared to observations 30.9% (18.1%) of the time for all clouds, 44.9% (36.3%) of the time for clouds with observed electric fields exceeding 100 V m^{-1}, and as high as 68.4% (48.3%) for clouds with moderate 85-GHz passive microwave signals over land and 71.2% (57.6%) with strong convective clouds.

These initial results suggest that it is, indeed, feasible to estimate the electric fields above electrified clouds from the passive microwave observations alone; however, there are a number of shortcomings in the algorithm that must be addressed. Future work will focus on taking into account differences in charge structure between convective and nonconvective clouds and to create a combined metric that uses the strengths of each frequency to provide a better estimate of electric field strength above a wide variety of storms.

Acknowledgments. This research was supported by NASA PMM Grant NNX13AQ70G under the direction of Dr. Ramesh Kakar and NASA Grant NNX08AK28G under the direction of Dr. Erich Stocker, as well as National Science Foundation Grant AGS-1135446. AMPR data were obtained from the NASA EOSDIS Global Hydrology Resource Center DAAC, Huntsville, Alabama.

REFERENCES

Adlerman, E. J., and E. R. Williams, 1996: Seasonal variation of the global electric circuit. *J. Geophys. Res.,* **101,** 29 679–29 688, doi:10.1029/96JD01547.

Bailey, J. C., and R. J. Blakeslee, 2006: Diurnal lightning distributions as observed by the Optical Transient Detector (OTD) and the Lightning Imaging Sensor (LIS). *Eos, Trans. Amer. Geophys. Union,* **87** (Fall Meeting Suppl.), Abstract AE33A-1050.

Bateman, M. G., M. F. Stewart, R. J. Blakeslee, S. J. Podgorny, H. J. Christian, D. M. Mach, J. C. Bailey, and D. Daskar, 2007: A low-noise, microprocessor-controlled, internally digitizing rotating-vane electric field mill for airborne platforms. *J. Atmos. Oceanic Technol.,* **24,** 1245–1255, doi:10.1175/JTECH2039.1.

Blakeslee, R. J., and Coauthors, 1999: Diurnal lightning distribution as observed by the Optical Transient Detector (OTD). 11th International Conference on Atmospheric Electricity, H. J. Christian Jr., Ed., NASA Conf. Publ. NASA/CP-1999-209261, 742–745.

——, D. M. Mach, M. G. Bateman, and J. C. Bailey, 2014: Seasonal variations in the lightning diurnal cycle and implications for the global electric circuit. *Atmos. Res.,* **135,** 228–243, doi:10.1016/j.atmosres.2012.09.023.

Blyth, A. M., H. J. Christian Jr., K. Driscoll, A. M. Gadian, and John Latham, 2001: Determination of ice precipitation rates and thunderstorm anvil ice contents from satellite observations of lightning. *Atmos. Res.,* **59–60,** 217–229, doi:10.1016/S0169-8095(01)00117-X.

Cecil, D. J., 2009: Passive microwave brightness temperatures as proxies for hailstorms. *J. Appl. Meteor. Climatol.,* **48,** 1281–1286, doi:10.1175/2009JAMC2125.1.

——, S. J. Goodman, D. J. Boccippio, E. J. Zipser, and S. W. Nesbitt, 2005: Three years of TRMM precipitation features. Part I: Radar, radiometric, and lightning characteristics. *Mon. Wea. Rev.,* **133,** 543–566, doi:10.1175/MWR-2876.1.

Deierling, W., and W. A. Peterson, 2008: Total lightning activity as an indicator of updraft characteristics. *J. Geophys. Res.,* **113,** D16210, doi:10.1029/2007JD009598.

Driscoll, K. T., R. J. Blakeslee, and M. E. Baginski, 1992: A modeling study of time-averaged electric currents in the vicinity of thunderstorms. *J. Geophys. Res.,* **97,** 11 535–11 551, doi:10.1029/92JD00857.

——, ——, and W. J. Koshak, 1994: A time-averaged current analysis of a thunderstorm using ground-based measurements. *J. Geophys. Res.,* **99,** 10 653–10 661, doi:10.1029/94JD00098.

Dye, J. E., and J. C. Willett, 2007: Observed enhancement of reflectivity and the electric field in long-lived Florida anvils. *Mon. Wea. Rev.,* **135,** 3362–3380, doi:10.1175/MWR3484.1.

——, and Coauthors, 2007: Electric fields, cloud microphysics, and reflectivity in anvils of Florida thunderstorms. *J. Geophys. Res.,* **112,** D11215, doi:10.1029/2006JD007550.

Halverson, J., and T. Rickenbach, 2002: Environmental characteristics of convective systems during TRMM-LBA. *Mon. Wea. Rev.,* **130,** 1493–1509, doi:10.1175/1520-0493(2002)130<1493:ECOCSD>2.0.CO;2.

——, and Coauthors, 2007: NASA's Tropical Cloud Systems and Processes Experiment. *Bull. Amer. Meteor. Soc.,* **88,** 867–882, doi:10.1175/BAMS-88-6-867.

Hollinger, J. P., J. L. Peirce, and G. A. Poe, 1990: SSM/I instrument evaluation. *IEEE Trans. Geosci. Remote Sens.,* **28,** 781–790, doi:10.1109/36.58964.

Hwang, P., 2012: Foam and roughness effects on passive microwave remote sensing of the ocean. *IEEE Trans. Geosci. Remote Sens.,* **50,** 2978–2985, doi:10.1109/TGRS.2011.2177666.

Jayaratne, E. R., C. P. R. Saunders, and J. Hallet, 1983: Laboratory studies of the charging of soft hail during ice crystal interactions. *Quart. J. Roy. Meteor. Soc.,* **109,** 609–630, doi:10.1002/qj.49710946111.

Kakar, R., M. Goodman, R. Hood, and A. Guillory, 2006: Overview of the Convection and Moisture Experiment (CAMEX). *J. Atmos. Sci.,* **63,** 5–18, doi:10.1175/JAS3607.1.

Kummerow, C., W. Barnes, T. Kozu, J. Shiue, and J. Simpson, 1998: The Tropical Rainfall Measuring Mission (TRMM) sensor package. *J. Atmos. Oceanic Technol.,* **15,** 809–817, doi:10.1175/1520-0426(1998)015<0809:TTRMMT>2.0.CO;2.

Lang, T. J., and S. A. Rutledge, 2008: Kinematic, microphysical, and electrical aspects of an asymmetric bow-echo mesoscale convective system observed during STEPS 2000. *J. Geophys. Res.,* **113,** D08213, doi:10.1029/2006JD007709.

Liu, C., E. Williams, E. J. Zipser, and G. Burns, 2010: Diurnal variations of global thunderstorms and electrified shower clouds and their contribution to the global electrical circuit. *J. Atmos. Sci.,* **67,** 309–323, doi:10.1175/2009JAS3248.1.

——, D. Cecil, and E. J. Zipser, 2011: Relationships between lightning flash rates and passive microwave brightness temperatures at 85 and 37 GHz over the tropics and subtropics. *J. Geophys. Res.,* **116,** D23108, doi:10.1029/2011JD016463.

——, ——, ——, K. Kronfeld, and R. Robertson, 2012: Relationships between lightning flash rates and radar reflectivity vertical structures in thunderstorms over the tropics and subtropics. *J. Geophys. Res.,* **117,** D06212, doi:10.1029/2011JD017123.

Mach, D. M., and W. J. Koshak, 2007: General matrix inversion technique for the calibration of electric field sensor arrays on aircraft platforms. *J. Atmos. Oceanic Technol.,* **24,** 1576–1587, doi:10.1175/JTECH2080.1.

——, R. J. Blakeslee, M. G. Bateman, and J. C. Bailey, 2009: Electric fields, conductivity, and estimated currents from aircraft overflights of electrified clouds. *J. Geophys. Res.,* **114,** D10204, doi:10.1029/2008JD011495.

——, ——, ——, and ——, 2010: Comparisons of total currents based on storm location, polarity, and flash rates derived from high-altitude aircraft overflights. *J. Geophys. Res.,* **115,** D03201, doi:10.1029/2009JD012240.

——, ——, and ——, 2011: Global electric circuit implications of combined aircraft storm electric current measurements and satellite-based diurnal lightning statistics. *J. Geophys. Res.,* **116,** D05201, doi:10.1029/2010JD014462.

Mansell, E. R., D. R. MacGorman, C. L. Ziegler, and J. M. Straka, 2005: Charge structure and lightning sensitivity in a simulated multicell thunderstorm. *J. Geophys. Res.,* **110,** D12101, doi:10.1029/2004JD005287.

Markson, R., 2007: The global circuit intensity: Its measurement and variation over the last 50 years. *Bull. Amer. Meteor. Soc.,* **88,** 223–241, doi:10.1175/BAMS-88-2-223.

Marshall, J. S., and S. Radhakant, 1978: Radar precipitation maps as lightning indicators. *J. Appl. Meteor.,* **17,** 206–212, doi:10.1175/1520-0450(1978)017<0206:RPMALI>2.0.CO;2.

Nesbitt, S. W., E. J. Zipser, and D. J. Cecil, 2000: A census of precipitation features in the tropics using TRMM: Radar, ice scattering, and lightning observations. *J. Climate,* **13,** 4087–4106, doi:10.1175/1520-0442(2000)013<4087:ACOPFI>2.0.CO;2.

Peterson, M. J., 2011: Satellite and ground based observations of lightning flashes in the stratiform and anvil regions of convective systems. M.S. thesis, Dept. of Atmospheric Sciences, University of Utah, 139 pages.

Prigent, C., E. Defer, J. R. Pardo, C. Pearl, W. B. Rossow, and J.-P. Pinty, 2005: Relations of polarized scattering signatures observed by the TRMM Microwave Instrument with electrical processes in cloud systems. *Geophys. Res. Lett.,* **32,** L04810, doi:10.1029/2004GL022225.

Reynolds, S. E., M. Brook, and M. F. Gourley, 1957: Thunderstorm charge separation. *J. Meteor.,* **14,** 426–436, doi:10.1175/1520-0469(1957)014<0426:TCS>2.0.CO;2.

Saunders, C. P. R., and S. L. Peck, 1998: Laboratory studies of the influence of the rime accretion rate on charge transfer during crystal/graupel collisions. *J. Geophys. Res.,* **103,** 13 949–13 956, doi:10.1029/97JD02644.

——, W. D. Keith, and R. P. Mitzeva, 1991: The effect of liquid water content on thunderstorm charging. *J. Geophys. Res.,* **96,** 11 007–11 017, doi:10.1029/91JD00970.

Smith, E. A., and Coauthors, 2007: International global precipitation measurement (GPM) program and mission: An overview. *Measuring Precipitation from Space,* V. Levizzani, P. Bauer, and F. J. Turk, Eds., Advances in Global Change Research, Vol. 28, 611–653, doi:10.1007/978-1-4020-5835-6_48.

Spencer, R. W., H. G. Goodman, and R. E. Hood, 1989: Precipitation retrieval over land and ocean with the SSM/I: Identification and characteristics of the scattering signal. *J. Atmos. Oceanic Technol.,* **6,** 254–273, doi:10.1175/1520-0426(1989)006<0254:PROLAO>2.0.CO;2.

——, R. E. Hood, F. J. LaFontaine, E. A. Smith, R. Platt, J. Galliano, V. L. Griffin, and E. Lobl, 1994: High-resolution imaging of rain systems with the Advanced Microwave Precipitation Radiometer. *J. Atmos. Oceanic Technol.,* **11,** 849–857, doi:10.1175/1520-0426(1994)011<0849:HRIORS>2.0.CO;2.

Stolzenburg, M., W. D. Rust, B. F. Smull, and T. C. Marshall, 1998a: Electrical structure in thunderstorm convective regions: 1. Mesocale convective systems. *J. Geophys. Res.,* **103,** 14 059–14 078, doi:10.1029/97JD03546.

——, ——, ——, and ——, 1998b: Electrical structure in thunderstorm convective regions: 2. Isolated storms. *J. Geophys. Res.,* **103,** 14 079–14 096, doi:10.1029/97JD03547.

Takahashi, T., 1978: Riming electrification as a charge generation mechanism in thunderstorms. *J. Atmos. Sci.,* **35,** 1536–1548, doi:10.1175/1520-0469(1978)035<1536:REAACG>2.0.CO;2.

——, and K. Miyawaki, 2002: Reexamination of riming electrification in a wind tunnel. *J. Atmos. Sci.,* **59,** 1018–1025, doi:10.1175/1520-0469(2002)059<1018:ROREIA>2.0.CO;2.

Toracinta, E. R., D. J. Cecil, E. J. Zipser, and S. W. Nesbitt, 2002: Radar, passive microwave, and lightning characteristics of precipitating systems in the tropics. *Mon. Wea. Rev.,* **130,** 802–824, doi:10.1175/1520-0493(2002)130<0802:RPMALC>2.0.CO;2.

Vivekanandan, J., J. Turk, and V. N. Bringi, 1991: Ice water path estimation and characterization using passive microwave radiometry. *J. Appl. Meteor.,* **30,** 1407–1421, doi:10.1175/1520-0450(1991)030<1407:IWPEAC>2.0.CO;2.

Whipple, F. J. W., and F. J. Scrase, 1936: *Point Discharge in the Electric Field of the Earth: An Analysis of Continuous Records Obtained at Kew Observatory.* Geophysical Memoirs, No. 68, Vol. 7, H. M. Stationery Office, 1–20.

Williams, E. R., 1989: The tripole structure of thunderstorms. *J. Geophys. Res.,* **94,** 13 151–13 167, doi:10.1029/JD094iD11p13151.

——, 2009: The global electrical circuit: A review. *Atmos. Res.,* **91,** 140–152, doi:10.1016/j.atmosres.2008.05.018.

Wilson, C. T. R., 1921: Investigation on lightning discharges and on the electric field of thunderstorms. *Philos. Trans. Roy. Soc. London,* **221A,** 73–115, doi:10.1098/rsta.1921.0003.

——, 1924: The electric field of a thundercloud and some of its effects. *Proc. Phys. Soc. London,* **37,** 32D, doi:10.1088/1478-7814/37/1/314.